Proceedings Paper:
El-Jummah, AM, Andrews, GE and Staggs, JEJ (2019) Predictions of Impingement Heat Transfer With Dimples, Pin-Fins and Zig-Zag Rib Obstacles: Conjugate Heat Transfer Computational Fluid Dynamics Predictions. In: Proceeedings of the ASME TurboExpo 2019 Volume 5A: Heat Transfer. ASME Turbo Expo 2019: Turbomachinery Technical Conference and Exposition, 17-21 Jun 2019, Phoenix, Arizona, USA. American Society of Mechanical Engineers. Article no: GT2019-90730. ISBN: 9780791858646.

https://doi.org/10.1115/gt2019-90730

Proceedings of ASME Turbo Expo 2019: Turbomachinery Technical Conference & Exposition
GT2019
June 17-21, 2019, Phoenix AZ, USA

GT2019-90730

Predictions of Impingement Heat Transfer with Dimples, Pin-fins and zig-zag rib Obstacles: Conjugate Heat Transfer Computational Fluid Dynamics Predictions

Abubakar M. El-Jummah
Department of Mechanical Engineering,
University of Maiduguri, 1 Bama Road,
P. M. B. 1069, Maiduguri
Borno State, Nigeria

Gordon E. Andrews and John E. J. Staggs
School of Chemical and Process Engineering,
University of Leeds, LS2 9JT
Leeds, West Yorkshire, UK

ABSTRACT

Regenerative cooling of low NO_x gas turbine combustors was investigated using impingement heat transfer with all the combustion air used for wall cooling prior to passing to the flame stabiliser. 10 rows of impingement holes were modelled. Three obstacles were compared with smooth wall impingement heat transfer. The CHT/CFD methodology used was that validated against experimental results in previous publications of the authors. The impingement heat transfer enhancement geometries investigated were circular pin-fins, dimples and zig-zag ribs, which were aligned transverse to the direction of the cross-flow on the impingement target surface. The obstacles were equally spaced on the centre-line between each row of impingement jets transverse to the cross-flow. One heat transfer enhancement obstacle was used per impingement jet air hole. The CFD calculations were carried out for an air mass flux G of 1.08, 1.48 and 1.94 kg/sm^{2}bara, which are the high flow rates used for regenerative combustor wall cooling. Comparison of the current CFD predictions and previous CFD work, that have experimental data, were made for the flow pressure loss and the surface and locally X^2 average HTC, *h*. It was concluded that none of the obstacles in the impingement gap a significant increase in the surface averaged heat transfer coefficient (HTC). The impact of the obstacles was to increase the flow maldistribution due to the increased pressure loss. This resulted is less heat transfer from the reduced air mass flow in the first 4 holes and increased heat transfer in the last 4 holes, relative to the smooth wall results. The main effect of the obstacles was to increase the heat transfer to the impingement jet surface. The dimpled surface was predicted to have a very poor performance, with significantly reduced impingement heat transfer. This was due to the impingement jets being deflected away from the target surface by the shape of the dimples and this reduced the surface heat transfer.

INTRODUCTION

The impingement geometry investigated was intended for use in low NOx primary zone combustion chamber wall cooling. The combustion air is used to cool the combustor walls prior to passing to the low NO_x flame stabiliser. This application is a high coolant mass flow rate, G kg/sm^{2}bara, with a low coolant pressure loss. There has to be sufficient air pressure available after the wall cooling to overcome the pressure loss at the low NO_x flame stabiliser for flame stability and fuel and air mixing purposes. Thus, there cannot be high velocity crossflow interactions with the obstacles in the crossflow as this would create a high coolant pressure loss. Impingement cooling is also used for cooling combustor transition ducts to the turbine inlet with the impingement air passed into combustor as film cooling or as part of the dilution air.

Abdul Husain and Andrews [3] reviewed the use of obstacles to enhance impingement heat transfer and most work had investigated the enhancement experimentally. The maximum heat transfer enhancement found experimentally was 20-50% [4] using several pin fins between the impingement jets. The present CHT CFD work investigates three main heat transfer enhancing obstacles that have been shown experimentally to enhance impingement heat transfer [1, 4-14]: circular pin-fins, zig-zag (or inclined) ribs and dimples in the target surface, with depth to dimple diameter, δ/D_o, of 0.3, as summarised in Table 1 and shown in Fig. 1.

El-Jummah and Andrews et al. [15-20] validated the computational methods used in the present work against experimental results. They investigated experimentally flat ribs and rectangular pin fins or slotted ribs, with co- and cross-flow of the coolant in the impingement gap. The CHT/CFD predictions [15 -17] were in good agreement with the experimental results, as illustrated in Fig. 2 for the mean surfaced averaged heat transfer coefficient. Good agreement was also found for the system pressure loss, which indicated that the aerodynamic predictions were correct. This research used the computational procedures validated in this earlier work, to explore design options for enhanced impingement heat transfer.

The impingement hole size, D, pitch, X, and impingement gap, Z, in this work were the same as for the smooth target impingement wall [21] as well as for previous predictions of impingement cooling with obstacles in the gap [17]. A 10 × 10 array of impingement jet holes was used with a fixed X/D of 4.66, Z/D of 3.06 and *n* of 4306 m^{-2}, as summarised in Table 2 [18, 21-23]. The range of G that was predicted was 1.08 - 1.93 kg/sm^{2}bara, the same as used by El-jummah et al. [22] for the smooth wall. Each coolant mass flow, G, requires a new computation, but no change in

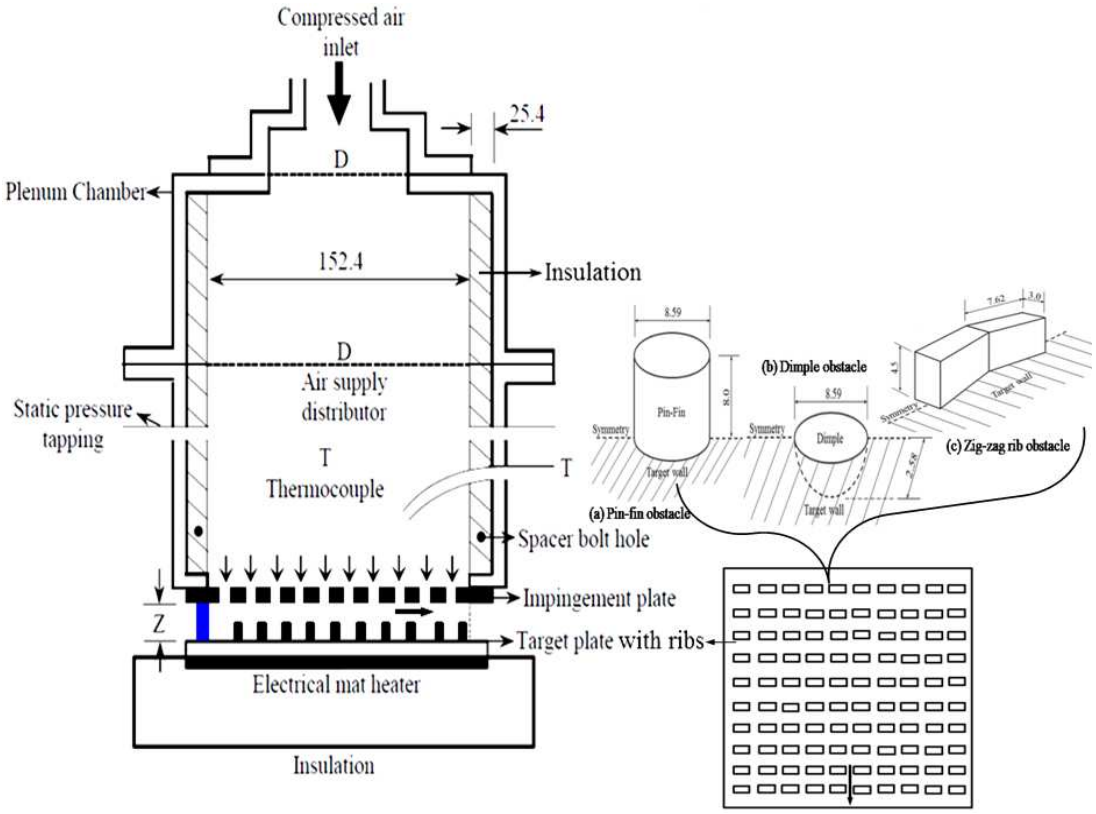

Figure 1: Impingement cooling experimental test rig with pin-fin (or dimple or zig-zag ribs) obstacles on the target surface

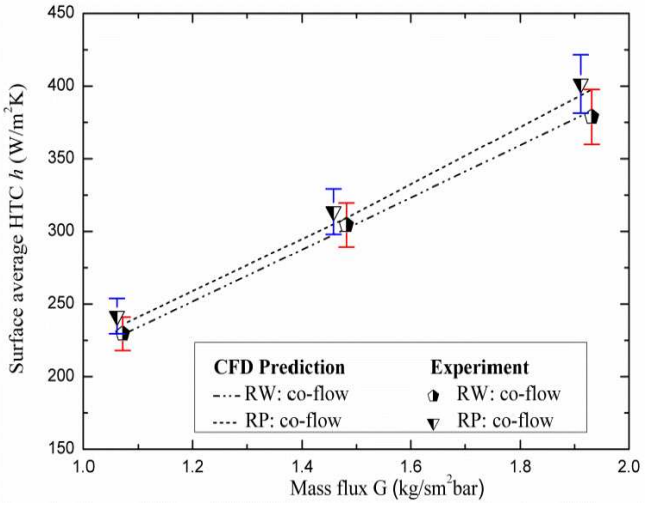

Figure 2: Impingement jet heat transfer coefficient on the enhanced target surface in co-flow configuration [15, 16]

Table 2: Geometrical Parameters

Variables	Dimensions
D (mm)	3.27
X (mm)	15.24
Z (mm)	10.0
L (mm)	6.35
L/D	1.94
X/D	4.66
Z/D	3.06
X/Z	1.52
n	4306 m^{-2}
Array	10 × 10

Table 1: Obstacle Walls Parameters

Types	W or D_o (mm)	H or δ (mm)	t (mm)	H/W δ/D_o
Zig-zag ribs	Continuous	4.50	3.0	
Pin-fin (circular)	8.59	8.00	-	0.93
Dimple	8.59	2.58	-	0.30

Table 3: Grid node distribution for y^+ ~35 for a total number of grids of about 1 million.

Types	Grid node distribution (%)			
	Test walls	Obstacles	Gap	Holes
Zig-zag ribs	28.5	8.3	19.5	8.4
Pin-fin (circular)	26.5	6.7	23.4	8.1
Dimple	22.8	5.7	27.4	8.8

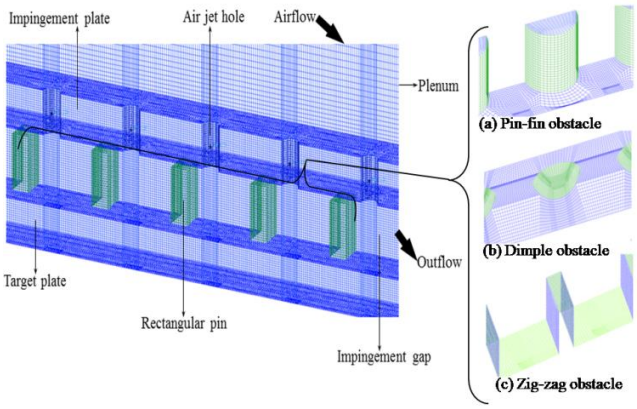

Figure 3: The impingement jet model grid geometry with obstacles: pin-fin, dimple or zig-zag on the target surface.

the grid geometry was needed. A new computational grid was required for each obstacle that was predicted. The present predictions on the effect of obstacles in the impingement gap was compared with the previous predictions for smooth and enhanced walls cooling to predict the enhancement of heat transfer [17, 21-23].

CFD METHODOLOGY

Model Grid Geometry

The impingement cooling geometry is shown in Fig. 1 and was the same as that modelled in the work of El-jummah et al [21, 22] for smooth target walls, as shown in Table 2. This work investigates the potential improvement in the heat transfer using the obstacles in the impingement gap in Table 2. The dimensions of the obstacles are shown in Fig. 1. The zig-zag ribs consisted of continuous ribs of height H, that was 45 % of the impingement gap, Z. The circular pin-fins had a height H that was 80 % of Z with equal pin-width, W. The dimple in the impingement surface in Figure 1 offers no obstruction to the crossflow, but changes the interaction of the impingement jet with the target surface, as the impingement jet was aligned with the dimple. This is likely to be the lowest influence of the geometry change on the pressure loss as the dimples do not block the crossflow.

These obstacles were investigated for the cross-flow normal to the obstacles. The blockage of the ribs was greater in the cross-flow direction and so the pressure loss increase was higher. The gap between the top of the circular pin-fins was to allow for thermal expansion, as the wall and rib are hotter than the impingement jet wall [18]. If there was a solid connection, differential thermal expansion could create thermal stresses and cracking.

The computational grid geometries (ANSYS ICEM) are summarised in Table 3. The dimpled obstacle of Figure 3c formed part of the target wall depth, this resulted in the impingement gap fluid grids replacing part of the target solid wall grids. It also increased the impingement gap cell size and reduced the target wall cells, as a proportion of the total computational cells, as in Table 3. The grid geometries for all the obstacles used about a million computational nodes. The number of cells in the plenum was fixed at 35.3 % of the total grids. The dimpled target surface was modelled with the dimples in-line with the impingement jet. The other obstacles grids were in the impingement gap, hence the obstacle solid walls replaced part of the impingement gap fluid grids as shown in Table 3. Also, the cross-flow obstacles were modelled using the whole obstacle width, as shown in Figure 3.

The approach that was used to model the zig-zig obstacle of Figure 3c is similar to that used experimentally for inclined ribs by Wang et al [1]. The zig-zag ribs were essentially a modification of the straight ribs used previously [19], but were only used with cross-flow. The use of inclined ribs to the cross-flow is common in enhanced heat transfer for duct flow [1] and this was applied to impingement cooling in this work. The circular pin-fin obstacle of Figure 3b was modelled as symmetrical, so that only half the pin diameter was required in the grid. This will be compared with the rectangular pin obstacle in cross-flow [15, 19].

Computational Procedures

The present CHT CFD investigations for the three types of obstacles modelled were computed for G of 1.08, 1.48 and 1.98 kg/sm^{2}bara respectively. Table 4 shows the model computational flow boundary conditions that were used. These flow conditions were the same as those used by El-jummah et al [15, 17, 22].

Table 4: Computational Flow Conditions

G (kg/sm^{2}bara)	1.93	1.48	1.08
V_j (m/s)	43.41	33.5	24.3
U_c(m/s)	24.0	18.4	13.4
V_j/U_c	1.8	1.8	1.8
$Re_h\left(=\rho V_j D/\mu\right)$	9680	7440	5400
T_∞(K)	288	288	288
T_w(K)	353	353	353
ρ (kg/m^3)	1.225	1.225	1.225

The standard k - ε turbulence model in ANSYS Fluent was used with a wall function y^+ value ~35 [15, 17], as shown in Table 3. These y^+ values have been reported in the range of the near wall using the law of the wall that is $30 < y^+ < 300$. This computational procedure was the same as that previously validated [21, 22 - 24]. This is because the flow aerodynamics in the impingement gap include strong flow recirculation, for which the k - ε model has good prediction capabilities.

The computational grids (ANSYS ICEM) with the addition of obstacles on the Target wall are shown in Figure 3 for three obstacle geometries and the smooth wall comparison. The minimum cell orthogonal quality and aspect ratio, for all the geometries modelled were fixed at 0.61 and 3.53, respectively. The numbers of cells in all the computational zones were shown to be adequate, which was based on the previously predicted grid sensitivity tests [17, 21, 23]. The number of computational grids used was about a million, the same as in the previous work of El-jummah et al. [15] for the continuous ribs and rectangular pin-fin ribs.

El-Jummah et al. [23] carried out a grid sensitivity study of an impingement configuration and found that for grid sizes greater than half a million there was little improvement in the predictions relative to the experimental measurements. In the present work about a million nodes were used for each geometry. The distribution of the computational nodes is summarised in Table 3 and Fig. 3. The convergence criteria were set at 10^{-5} for continuity, 10^{-11} for energy and 10^{-6} for k, ε and momentum (x, y and z velocities), respectively. The second-order and first-order discretization schemes for the momentum and TKE/dissipation used the PISO schemes that were based on PRESTO applications.

PREDICTIONS OF THE AERODYNAMICS

The aerodynamics in the impingement gap are complex, as shown by El-jummah et al. [15, 17] using CHT/CFD modelling. The additions of obstacles to the target wall was aimed at enhancing the heat transfer and were placed at the location of the reverse flow between each impingement jet. The inclusion of the obstacle increases the complexities of the aerodynamics, as the crossflow increases with succesive rows of impingement jets. This flow complexity is shown in the velocty pathlines of Figure 4 (a - c) and are compared with the smooth target surface in Figure 4d.

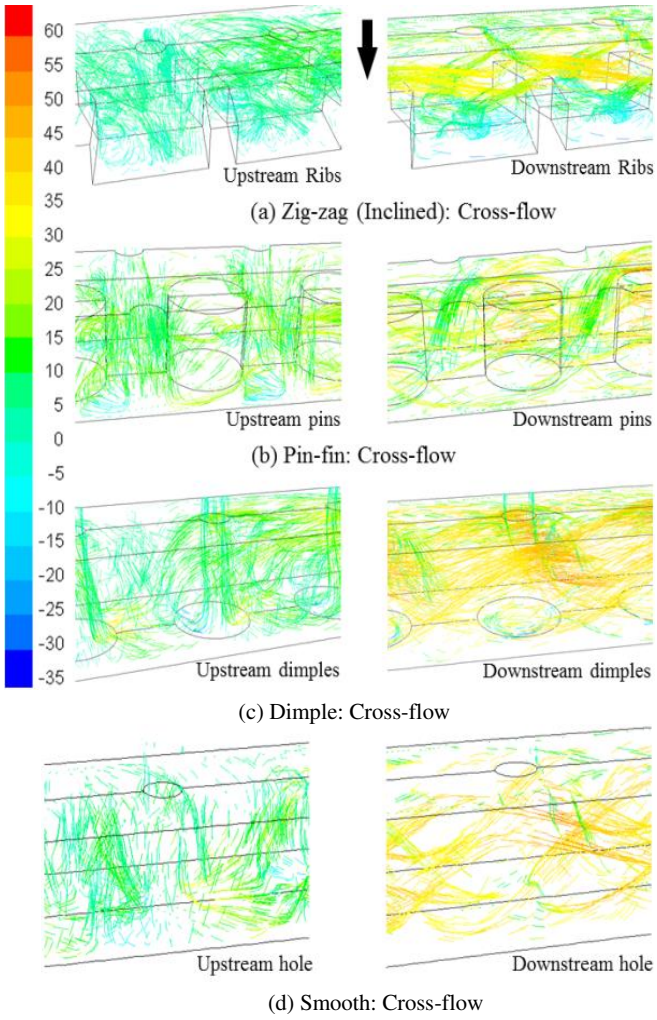

Figure **4:** Velocity (m/s) pathlines in the impingement gap

The aerodynamics for the first two and the last two impingement holes are shown in Fig. 4 as upstream and downstream aerodynamics. Figure 4 shows that the obstacles were placed to have convective heat transfer from the reverse impingement flow for the first few holes. However, as the crossflow increased in magnitude in the downstream region of the impingement gap, the deflection of the impingement jet by the crossflow reduced the beneficial effect of the obstacles in terms of the enhanced obstacle surface crossflow.

For cross-flow over the inclined zig-zag ribs, there was a significant change in the aerodynamics, as shown in Figure 4a. Vortices were predicted to be created between the ribs due to the reverse flow jet deflection. This gives the cross-flow a complex interaction with the next impingement jet and with the rib inclination. By the downstream rib after 10 holes, there was little flow in the wall region and the cross-flow was all across the impingement jet surface [18].

The circular pin-fins have the edge of the impingement jet close to the surface of the pin-fins, as in Figure 4b, and potentially this should enhance the heat transfer. With the circular pin-fins in cross-flow, the cross-flow at the downstream end of the gap shows that the flow velocity is high between the pins and recirculates behind them. This is a potential additional surface heat transfer mode around the pin-fins. It will be shown that these cylindrical pin fins had the highest HTC of all the obstacles investigated, but still not significantly better than the smooth wall.

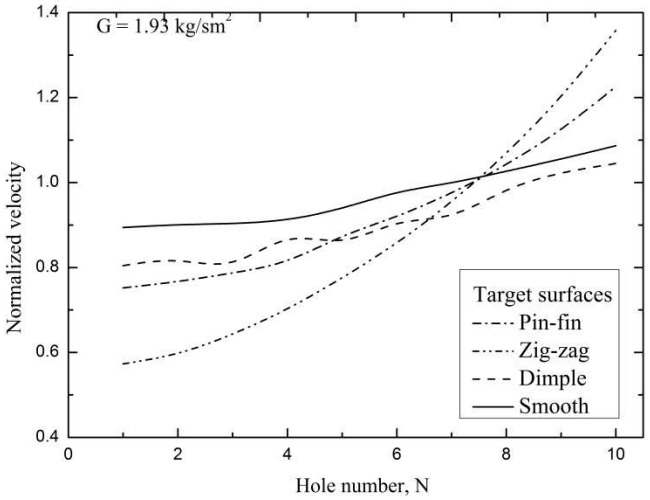

Figure 5: Flow-maldistribution in the impingement jet holes

The dimple obstacles in Figure 4c show that the dimples create a stronger reverse flow of the impingement jet and reduce the surface flow between the impingement jets. This will be shown to lead to a reduced surface heat transfer. Potentially, this stronger reverse flow is a greater resistance to the cross-flow deflection of the impingement jet flow. However, comparison of Figs 4c and 4d for the smooth surface shows a very similar large jet flow deflection in the downstream region.

In the downstream part of the flow in Figure 4, the aerodynamics were dominated by the crossflow between the pin-fins cylinders. The zig-zag rib has similar aerodynamics to the flat rib in crossflow [15], but there is evidence of a difference in the downstream vortex structure, which may be beneficial to heat transfer enhancement.

The impact of the crossflow in the impingement gap is to induce a flow maldistribution between the first and last impingement holes, due to the pressure loss created by the crossflow. Figure 5 shows the predicted flow maldistribution, with a comparison with that for the smooth wall. This clearly shows that the zig-zag ribs, the circular pin fins and the dimples all increased the flow maldistribution, relative to that for a smooth wall. This is due to the additional pressure loss caused by the interaction of the crossflow with the obstacles. The increase in the flow maldistribution was predicted to be greatest for the zig-zag ribs, as these span the whole of the crossflow. The circular pin fins have the next greatest impact, even though they leave a clear gap between the pins. The most surprising prediction is that the dimples make the flow maldistribution worse than for the smooth wall, even though there is no increase in the crossflow blockage. The greater flow reversal and reduced target surface flow, shown in Fig. 4c, must give a greater resistance to the crossflow, which then increases the flow maldistribution.

Predictions of the Axial Pressure Loss Profiles

The obstacles create a blockage to the cross-flow which was predicted to increase the pressure loss, as shown in Figure 6. This is the cause of the increased flow maldistribution shown in Fig. 5. Figure 6 shows that the zig-zag ribs had the greatest increase in the pressure loss as they had the greatest blockage to the flow. The cylinderical pin-fins were also predicted to have higher $\Delta P/P$ than for the smoothwall, but their round end facing the crossflow reduced the increase in pressure loss compared with the sharp edged zig zag ribs. The dimpled wall, was predicted

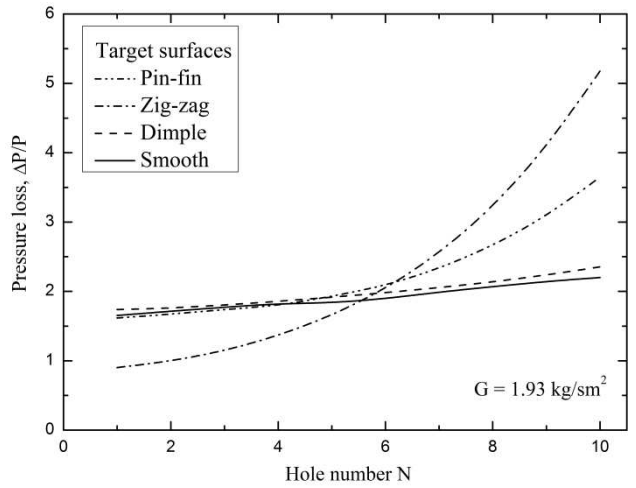

Figure 6: Predicted impingement wall pressure loss ΔP/P%

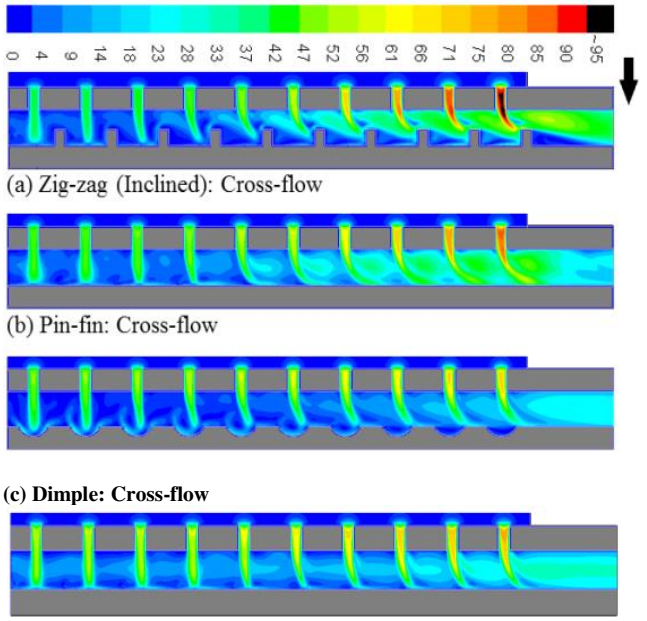

(i) Rows of half holes symmetry plane

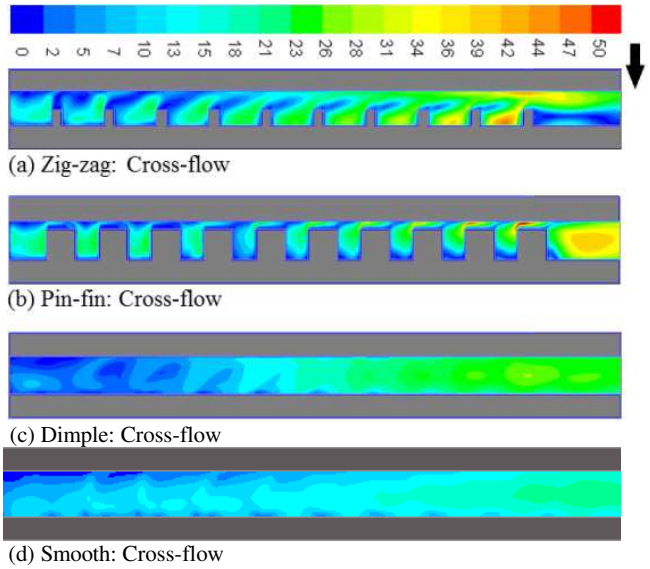

(ii) Symmetry plane between rows of holes

Figure 7: Impingement gap contours of flow velocity (m/s) for G of 1.93 kg/sm^{2}bara with X/D of 4.60 and Z/D of 3.06.

to have a very similar pressure loss to the smooth wall, which was expected as there was no increased blockage to the cross-flow.

Predictions of the Velocity Profiles

The velocity profile in the direction of the impingement jet flow is shown for all the geometries investigated in Fig. 7 for (i) the symmetry planes of the impingement jet and (ii) the plane between the holes. The flow-maldistribution between the holes, as shown in Figure 5, is also shown in Fig. 7 with higher velocities in the last jet compared with the first jet due to the effect of the cross-flow. The influence of the obstacles compared with the smooth wall is for the flow maldistribution to become greater. Fig. 7(i) shows that with the zig-zag fins the highest velocity is created in the last hole and the lowest in the first hole. For the zig-zag ribs in cross-flow, the deflection of the jet by the high cross-flow velocity over the ribs is much higher than for the smooth wall. These deflected jets impinge on the upstream face of the ribs after the third row of hole and this will produce good cooling there, at the expense of reduced cooling on the target surface. Fig. 7(ii) shows the predicted flow in the crossflow direction between the impingement jets. The recirculated jet is strongly deflected by the crossflow and this was predicted to be worse for the high blockage ziz-zag ribs.

The circular pin-fins in Figure 7(i)(b) has a high jet deflection by the locally high cross-flow velocity between the pins. The pin-fins have the pins in the crossflow and produce a large blockage, which gives poor flow around the pins so that the heat transfer surface area of the pins is not well utilised, as shown in Figure 7(ii)(b).

The dimpled surface in Figure 7(i) had a strong upstream flow recirculation out of the dimple. This would give additional surface heat transfer inside the dimple. Compared with the smooth surface the dimples increased the reverse flow of the impingement jet and removed it from the downstream surface, which will lead to reduced surface heat transfer. This was also noted in the flow patterns in Fig. 4. It will be shown later that the net result is very little enhancement of heat transfer overall for this geometry. As the cross-flow from the upstream impingement jets increase, the impingement jet deflection forced the impingement jet out of the dimple and there was then no benefit of the dimple after the seventh hole.

Predictions of the Turbulent Kinetic Energy Profiles

The turbulent kinetic energy (TKE) on the wall surface controls the wall heat transfer [4, 21 - 23]. Figure 8 shows the predicted TKE in the symmetrical plane in line with the impingement jets for the obstacles and compares them with the smooth wall TKE. Figure 9 shows the predicted TKE distribution on the target surface. These predictions show that the action of the obstacle is to reduce the turbulence on the surface and to move the peak turbulence to the obstacle surface. This is most clearly shown for the zig-zag ribs in Figure 9. The only surface roughness that increases turbulence on the target wall is the dimple target surface, but most of the heat transfer is inside the dimple recess in the target wall and the turbulence on the suface around the dimple is reduced relative to the smooth wall.This enhanced TKE in the dimple recess surface is only for the first five dimples, as after this the impingement jet is deflected out of the dimple by the cross-flow.

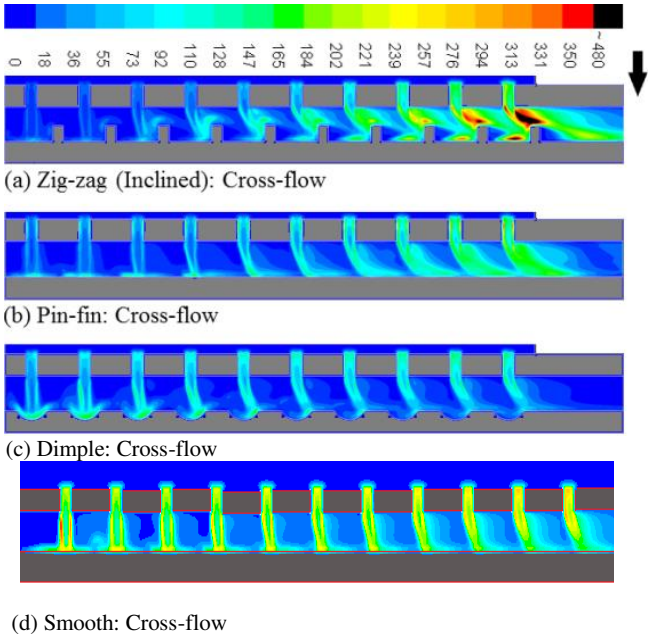

Figure 8: Contours of turbulent kinetic energy TKE (m^2/s^2) in the impingement gap row of half holes symmetry plane for G of 1.93 kg/sm^{2}bara

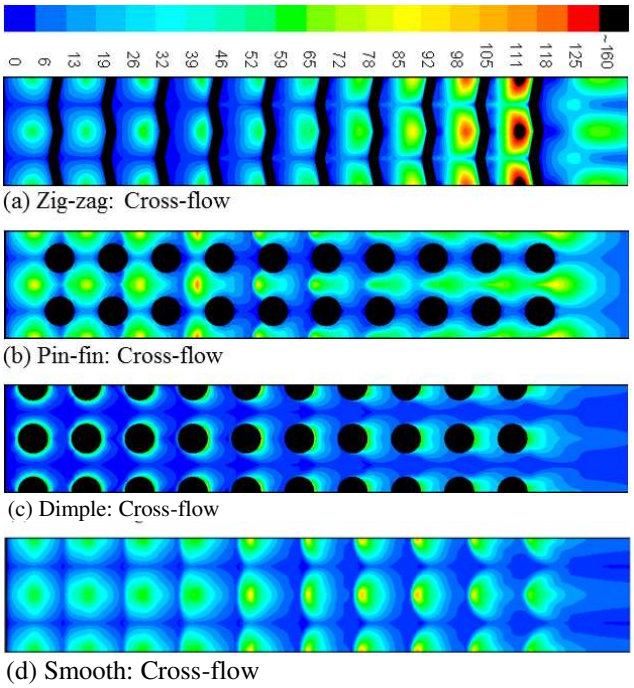

Figure 9: Predicted surface average turbulent kinetic energy TKE (m^2/s^2) on the enhanced target surface for G of 1.93 kg/sm^{2}bara.

The distribution of TKE on the target wall are shown in Figure 9. Clearly the flow-maldistribution with cross-flow in Figure 6, is that the zig-zag ribs results in a very high surface TKE for the downstream jets and is expected to have the same influence on the HTC. However, the greater deflection of the impingement jets reduces the target surface turbulence. The circular pin-fins in cross-flow were predicted to have low turbulence in the central region of the wall, but increased turbulence at the leading and trailing edge. This was due to the greater deflection of the impingement jet by the higher local cross-flow velocity between the pins.

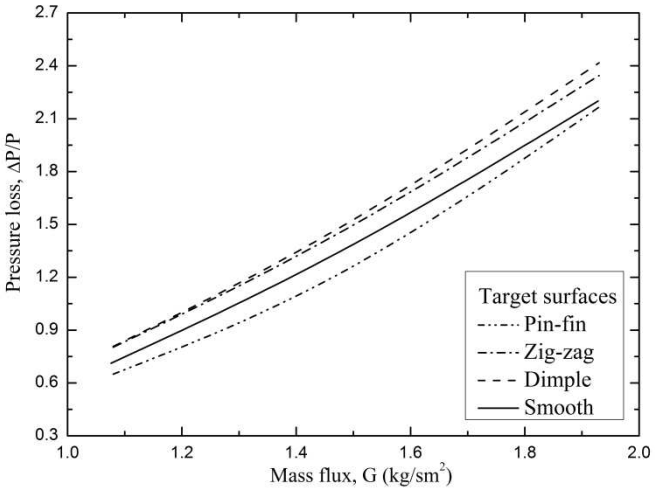

Figure 10: Comparison of the predicted impingement gap flow exit pressure loss for types of rough walls of varied G.

Predictions of the Overall Pressure Loss, ΔP/P%

The experimental pressure loss results for a smooth wall have been shown previously to have good agreement with the CHT/CFD predictions, using the present computational methods [20, 21, 23]. To achieve this agreement the experimental measurement configuration had to be modelled precisely. In the experiments the impingement cooled duct had a discharge length of 25mm before discharge to the atmosphere. On three sides this flange was used to bolt the test section to the impingement wall with the spacer gap, Z, and this also sealed the gap from air leaks on three sides. On the flow exit side no bolts were present and the gap was open. This extended outlet region is shown on the predictions in Figs. 7-9. Figure 7 shows that there was flow expansion to the full width of the duct with associated static pressure recovery in the 25mm outlet section. This was particularly strong for the rib and pin-fin obstacles, as shown in Fig. 7(i). The pressure loss was taken as the static pressure difference between the plenum chamber and the wall static pressure between the impingement jets at the exit of the 25mm duct. The experimental results were also corrected for the one dynamic head pressure loss that occurs at the dump expansion from the duct in the experimental test rig, this expansion was not modelled in this work. Without this additional section in the computation, the agreement between the predicted and measure pressure loss was poor (20, 21, 23). In the present work this outlet section was included, so that comparison with previous work could be made (15-17).

The predictions of the axial variation of the pressure loss across the impingement wall in Fig. 6 were determined as the difference in the plenum chamber air supply static pressure and the impingement wall static pressure between adjacent impingement holes for the same axial location. At the last hole this did not include the flow expansion downstream and static pressure recovery in the outlet duct. Thus, the predictions in Fig. 6 should not be compared with those in Fig.10.

The overall pressure loss predictions in Fig. 10 show a relative modest influence of the investigated obstacles in the gap relative to the smooth wall. This is desirable as any increased surface heat transfer should not be achieved with the penalty of drastically increased pressure loss. Figure 10 shows that the dimples had the greatest influence on the pressure loss, which was not expected as they offer no physical blockage to the flow.

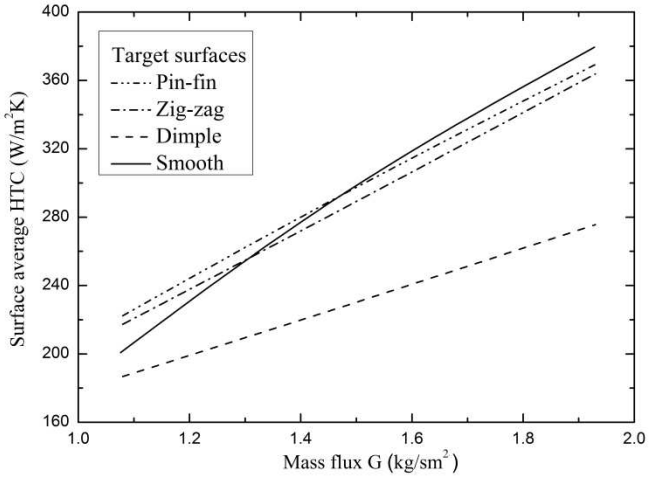

Figure 11: Comparison of predicted surface heat transfer coefficient on the enhanced target walls for varied G

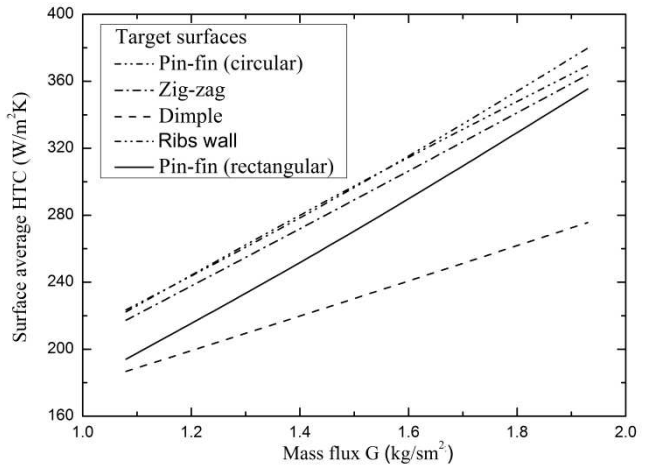

Figure 12: Comparison of previously [15 - 17] and the present predicted surface HTC on the enhanced target walls

The increased pressure loss for the dimples was due to the aerodynmically increased blockage due to the strong reverse flow. This aerodynamic blockage was a reverse flow jet greater than the dimple diameter, as shown in Fig. 7(i) for the first few hole. However, the increase in pressure loss for the dimples was relatively small and the cylindrical pin-fins also has a similar low pressure loss increase. The main pressure loss is at the impingement jet walls, as shown in Fig. 6, and the obstacles in the relatively low velocity crossflow had a lesser effect. The decrease in the pressure loss for the zig-zag ribs was not expected, as the flat ribs had shown in increase in pressure loss (15-17). This shows an aerodynamic benefit of the inclined ribs relative to the crossflow compared with normal ribs, which has been know in the turbine blade cooling literature for many years [1].

PREDICTIONS FOR SURFACE HEAT TRANSFER

The Surface Average HTC for varied G.

El-jummah et al. [15, 17] have shown good agreement between measurements and predictions, using the same methodology as in this work, for the surface averaged HTC with impingement heat transfer. They investigated experimentally and with CHT/CFD two obstacles in co-flow and cross-flow of the same experimentally designed configurations of continuous ribs and rectangular pin fins. The present work used the same approach to predict the influence of three different obstacles on the surface average HTC and on the axial trends of the X^2 surface averaged HTC. Figures 11 and 12 show the predictions for the surface average and the X^2 average HTC are shown in Figs. 13 and 14. Comparison with the smooth surface results are included in these Figures [20, 21, 23].

Figure 11 shows that the zig-zag fins and the cylindrical pin-fins were predicted to have a surface averaged heat transfer coefficient, HTC, close to that of the smooth surface. The HTC was higher at low G and lower at high G, but this difference was only 10% of the smooth wall values. Figure 12 shows the present obstacle results compared with the previous work of the authors (3, 15-19) for different obstacles in the same impingement configuration with crossflow. This shows that the present cylindrical pin-fins were predicted to be superior to the rectangular pin-fins (or slotted rib) used previously. Also the present zig-zag ribs were slightly better than the flat ribs of the same height in the previous work. However, as these were little different from the smooth wall, as shown in Fig. 11, it may be concluded that none of the present or previous obstacle geometries offered significant improvements in the heat transfer on a surface average HTC basis.

In contrast the dimpled surface was predicted to have a significant deterioration in the surface average heat transfer, especially at high G where the predictions were 26% below those for the smooth surface. This was also significantly worse than any previous studied obstacle (3, 15-19), as shown in Fig. 12. The reason for the deteriorated surface average HTC was due to the dimple increasing the reverse

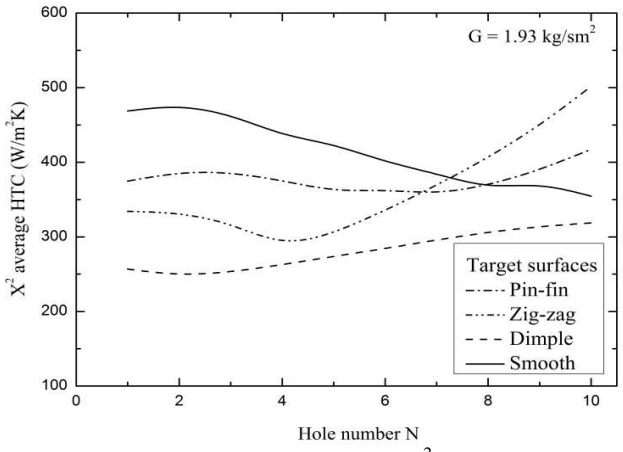

Figure 13: Comparison of predicted X^2 average HTC, *h* on the enhanced target surface for G of 1.93 kg/sm^{2}bara.

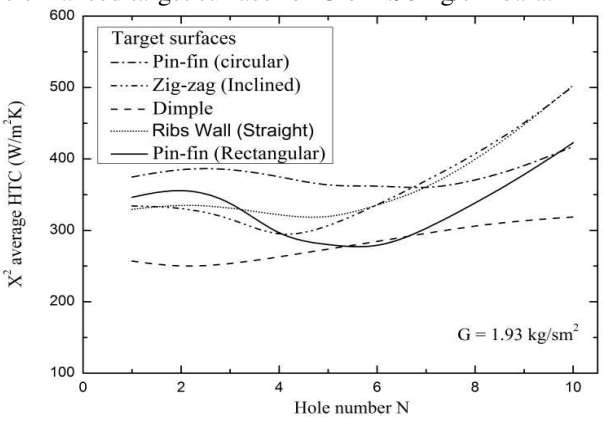

Figure 14: Comparison of previously [15 - 17] predicted and the present X^2 locally average HTC, *h* on the enhanced target surface for G of 1.93 kg/sm^{2}bara.

flow of the jets and deflecting the jets away from the cooled surface, as shown in Fig. 7. Also the TKE was convected away from the surface to be cooled, as shown in Fig. 8.

Figure 14 compares the present predictions with those for the previous obstacle geometries (15-17). The present zig-zag ribs were predicted to be close to the flat continous rib, but between holes 2-5 were slightly lower. Thus there was no heat transfer advantage of the inclined ribs used in the zig-zag format. The best results in Fig. 14 were for the present cylindrical pin fins, which were significantly better than the previous (15-17) rectangular pin fins, but still worse that the smooth wall.

The axial variation in the X^2 Average HTC at G = 1.93 kg/sm^{2}bara

The predicted surface averaged HTC over the X^2 area cooled by each impingement jet has been shown in previous work to agree with experimental measurements of the axial variation in the locally average HTC (15-17, 20-23). The present predictions of the influence of different obstacles on the axial variation of the X^2 surface average HTC are shown in Fig. 13 and compared with the previous obstacles in Fig. 14. Fig. 13 shows that there were significant differences in the axial variation of locally surface averaged HTC. All the obstacles had worse local HTC for the first six holes in the crossflow. Part of the reason for this was the flow maldistribution shown in Fig. 5. The extra crossflow pressure loss created by the obstacles caused the first four impingement holes to have lower air mass flow than the last four. This reduced the HTC for the first four holes and increased it for the last four holes, with little change in the average HTC compared with a smooth wall.

The zig-zag fins had higher local HTC for the last three holes, but this was not sufficient to compensate for the lower HTC over the first seven holes. The cylindrical pin-fins also had higher HTC for the last two holes, but lower HTC for the first eight holes, compared with the smooth wall. However, the axial variation in the HTC was much less. The dimpled surface was worse at all axial locations than the smooth wall and the two other obstacles. There was also only a small axial gradient in the local HTC, with a small increase in the downstream part of the crossflow.

For the first four holes all the obstacles were predicted to have much lower local surface averaged heat transfer than for a smooth wall. This was 50% lower for the dimpled surface and 20% lower for the cylindrical pin-fins.The main benefit of the obstacles was in the downstream part of the crossflow in the impingement gap, when the crossflow velocity had increased due to the flow outlet from the upstream jets and higher velocity impingement jets were created due to flow maldistribution.

However, this downstream increase was never sufficient to overcome the large deterioration in HTC for the first four holes. Part of the reason for this was the worse flow maldistribution, so that the first holes had less air than the downstream holes and this maldistribution was worse with obstacles compared with the smooth wall. An additional reason for this effect was that with the smooth wall two adjacent impinging jets flow along the flat surface between them and impinge and create a reverse flowing jet from the surface to the impingement jet wall, as shown in Fig. 7(i). When obstacles are placed between the holes this surface interaction is stopped. The result of this lack of interaction between the jets with obstacles is lower turbulence and lower HTC, as shown in Figs. 7-9. For a smooth wall with a

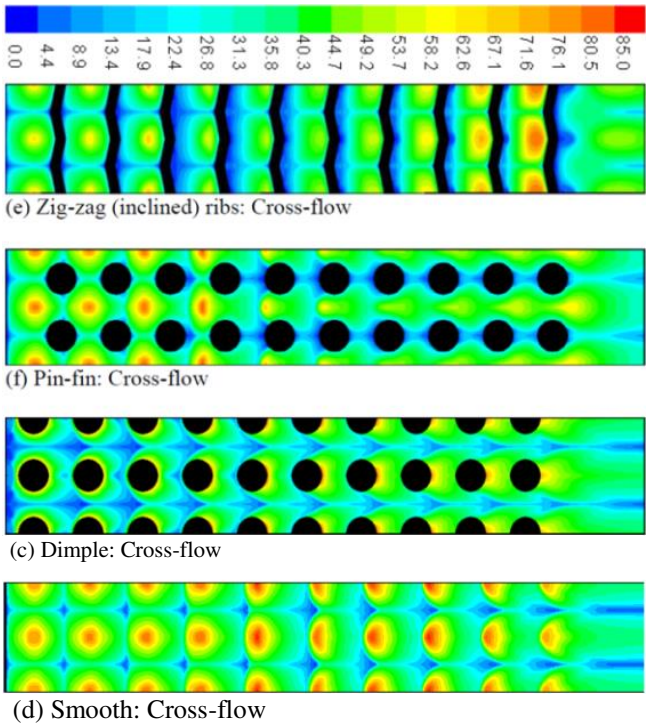

Figure 15: Contours of Nusselt number on the enhanced target surface for G of 1.93 kg/sm^{2}bara

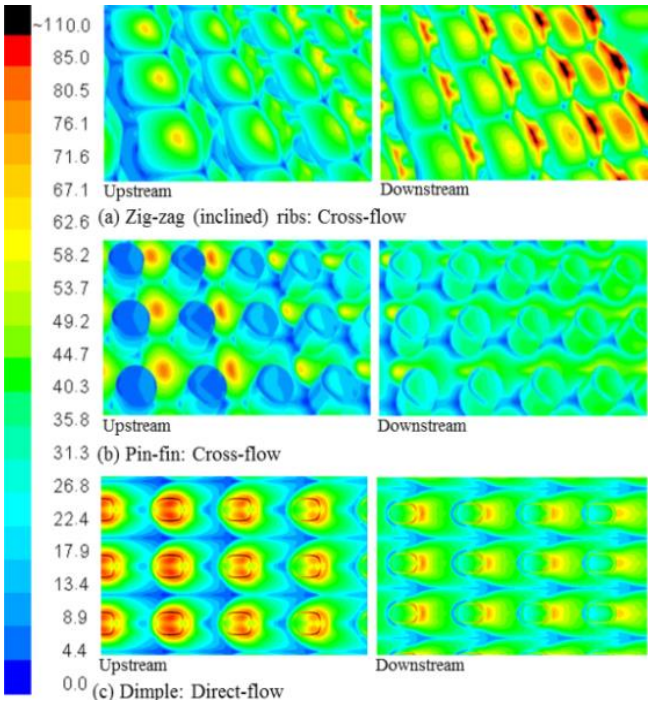

.

Figure 16: Contours of Nusselt number on the target surface with obstacle walls for G of 1.93 kg/sm^{2}bara

significant crossflow the impingement jets are deflected and by the fifth row of holes this interaction has ceased, as shown in Fig. 7(i). It is then in the downstream part of the impingement gap that the action of the obstacles is to create aerodynamic interactions with the crossflow that leads to an increase in local HTC.

Distribution of Target Surface Nusselt Number

Figure 15 shows the CHT/CFD predicted surface distribution of Nusselt number, Nu, on the target surface.

The smooth wall Nu distribution shows a much larger surface area with high Nu than for all the obstacles investigated. One of the actions of the obstacle is to block the surface from being cooled, by the area occupied by the obstacles which is greatest for the cylindrical pin fins. There is heat transfer from the obstacles and by conduction this cools the surface, but the evidence is that this is an inefficient process. Figure 15 is very similar to that for the distribution of TKE in Figure 9, which further explains the control of TKE in enhancing heat transfer.

The reduced surface heat transfer with the obstacles in place is partially compensated for by the heat transfer on the pin-fin surface, which extracts heat from the target surface by conduction. For the dimples the enhanced surface heat transfer inside the recess is part of the overall heat transfer. The predicted surface distribution of Nu are shown in Fig. 16. For the zig-zag ribs the surface heat transfer is low for the first few holes and does not compensate for the high surface heat transfer that the smooth surface impingement of adjacent jets create. The pins do have a high surface heat transfer in the downstream part of the crossflow, due to the action of the crossflow interacting with the ribs.

The surface heat transfer for the pin-fins is poor, as shown in Fig. 16. The impingement jets have a high local surface heat transfer between the pins for the upstream three jets. However, even here the impingement flow does not strongly interact with the cylinders to give high local Nu on the cylinder surface. In the downstream part of the flow the cylinders increase the crossflow velocity, but this does not result in high heat transfer to the cylindrical pins.

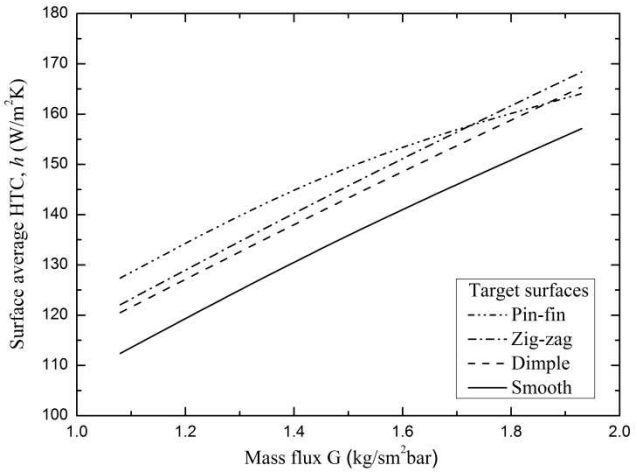

Figure 17: Comparison of the predicted HTC on the impingement jet wall for varied G.

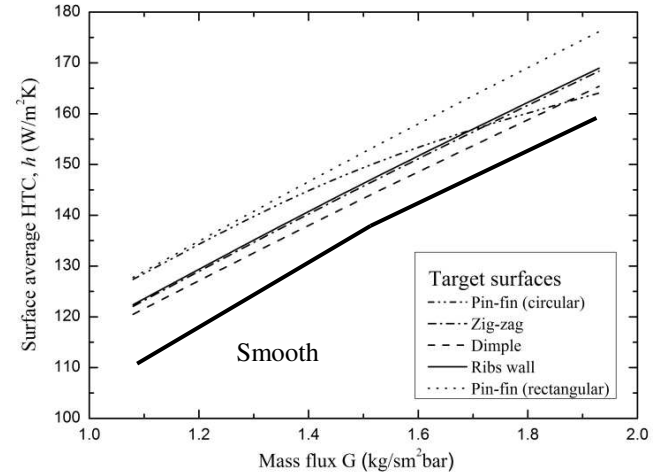

Figure 18: Comparison of previously [15 - 17] predicted HTC and present prediction for heat transfer to the impingement jet wall for varied G.

Heating of the Impingement Jet Wall

The aerodynamics of impingement jet arrays with a narrow gap are that there is a flow reversal on the centreline between each group of 4 holes in a square array [20-23]. This is shown in Fig. 4 for the first two impingement holes. This reverse flow jet is heated by the heat transfer at the target wall surface and this heated jet impinges on the impingement jet wall and heats it. Very few measurements have been made of this component of the heat transfer in impingement cooling. The action of obstacles can be to interfere with this reverse flow jet, particularly if the obstacle is placed where the reverse flow jet occurs, as it was for the cylindrical pins and the zin-zag ribs. Also a key action of the crossflow is to deflect the reverse flow jet, as can be seen by comparing the flow for the first two holes with the last two holes in Fig. 4. This has been previously reported by the authors [20-23] and others [6, 10] and has been shown to influence the effectiveness of the target wall cooling.

Figure 17 shows the impingement jet wall surface averaged HTC as a function of G for the three obstacles investigated with a comparison with the smooth wall results. The heat transfer is significant and is roughly 50-60% lower than the impingement target wall HTC in Fig. 11. Fig. 17 shows that a key effect of all the obstacles is to increase the heat transfer to the impingement jet surface compared with that for the smooth wall. This occurs with deterioration of the heat transfer to the target surface, as shown above.

The greatest increase in the heat transfer to the impingement jet surface was predicted to be that for the zig-zag ribs. Figure 18 compares the heat transfer predictions for the impingement jet surface in the present work with previous predictions for other obstacles [15-17]. This also shows that all obstacles in the impingement gap increase heat transfer to the impingement jet surface and the greatest increase was for rectangular pin fins, which had higher HTC at high G than the present predictions for zig-zag ribs. The dimples had the lowest increase in the HTC for the impingement jet surface compared with the smooth surface and this would be because they did not physically block the crossflow, but they did increase the reverse flow of the impingent jets.

The heating of the reverse flow jets can be used to visualise the reverse flow and the predictions of this are shown in Fig. 19, in a dimensional temperature form. Also shown here is the cooling of the target wall and the thermal gradients in the wall that will be discussed later. Figure 19 shows that for the smooth wall there was a clear reverse flow jet that was deflected by the crossflow in the downstream part of the impingement flow along the gap. The enhancement of this reverse flow is also clearly shown for the dimple surface. The physical presence of the cylindrical pins and the zig-zag ribs interferes with the reverse flow jet and are heated by it for the first few holes.

Figure 20 shows the predicted locally X^2 averaged HTC for the impingement jet wall as a function of the distance or hole number in the axial direction. This shows that the smooth wall had the highest HTC to the impingement jet wall for the first four holes and then it deteriorated relative to the geometries with obstables. Clearly the higher overall

$$T^* = \frac{(T - T_\infty)}{(T_w - T_\infty)}$$

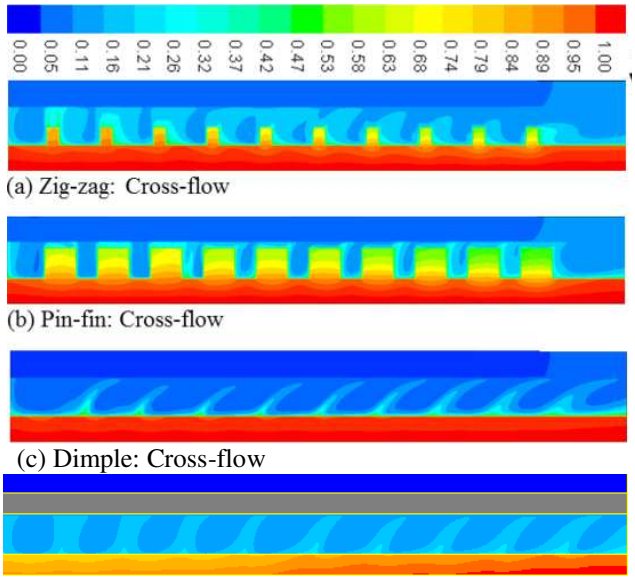

(a) Zig-zag: Cross-flow

(b) Pin-fin: Cross-flow

(c) Dimple: Cross-flow

(d) Smooth: Cross-flow

Figure 19: Contours of normalized temperature in the impingement gap for G of 1.93 kg/sm^{2}bara

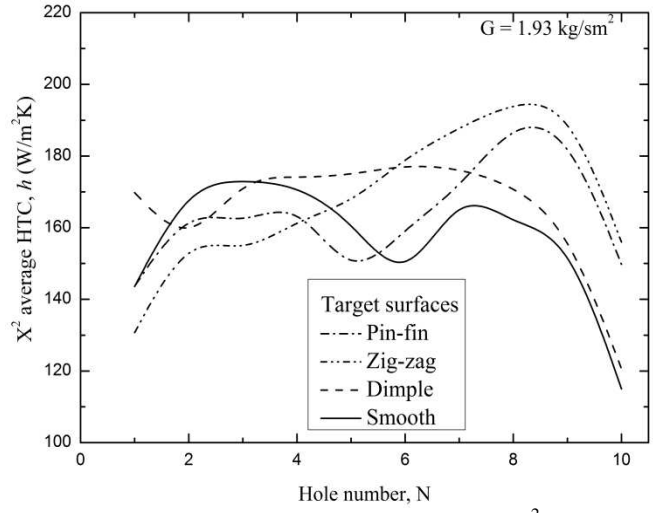

Figure 20: Comparison of predicted locally X^2 average HTC on the impingement jet plate for G of 1.93 kg/sm^{2}bara

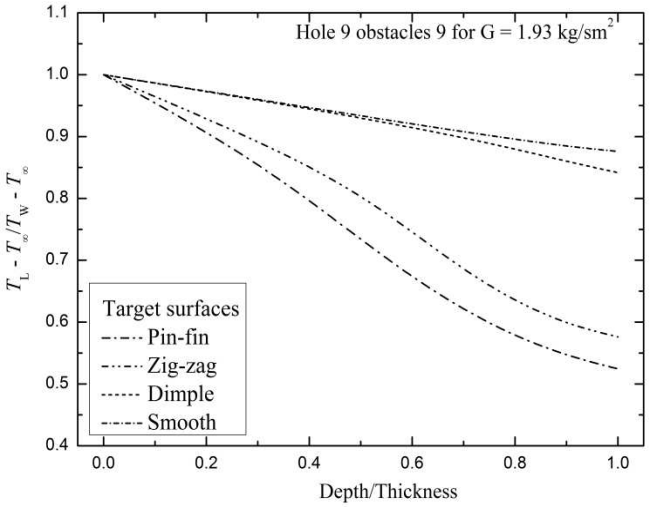

Figure 21: Comparison of predicted normalized temperature in the target wall for hole 9.

surface averaged HTC in Figs. 17 and 18 was due to the higher HTC after impingement jet row 4. The reason for this is that the obstacles are placed in the plane of the reverse flow and this deteriorates the reverse flow HTC on the impingement jet surface for holes 1-4. However, beyond this the crossflow velocity increases and this deflects the reverse flow jet and reduces the impingement jet wall heat transfer for the smooth wall. However, for the walls with obstacles the obstacles limit the reverse flow jet deflection, as shown in Fig. 19, and this increases the impingement jet wall local HTC over the last 6 holes of the impingement outflow.

Temperature Gradients in the Target Wall and Fins

Figure 19 shows the target wall surface distribution of normalised temperature T^* for all the obstacle walls and the smooth target wall. A high impingement target surface local HTC will give greater thermal gradients as it is extracting more heat. The greatest thermal gradient occur in the fins and pins, with the highest gradients in the cylindrical pins in Fig. 19. However, it is heat extraction from the target wall that is required and the thermal gradients here are greatest for the smooth wall over the first few rows of impingement jets. This is where the local heat transfer coefficients are greatest as shown in Figs. 13 and 15.

Figure 19 shows that the obstacles were predicted to have their greatest impact on thermal gradients over the last few rows of holes. Fig. 21 compares the thermal gradients at the ninth hole position and shows that the smooth and dimpled target walls gave the highest surface distribution of T^*. Figure 21 show that the pin-fin wall was predicted to have the highest temperature gradient and it had the highest HTC at hole 9 in Fig. 13. The smooth and dimple target surfaces had the lowest X^2 surface averaged HTC at hole 9 and these had the lowest thermal gradients in Fig. 21.

CONCLUSIONS

CHT/CFD predictions were used to try to improve the efficiency of regenerative wall cooling for low NO_x combustors using obstacles in the impingement gap, Z. Air coolant fluxes, G, from 1-2 kg/sm^{2}bara were investigated as these are representative of combustor wall cooling using all the combustion air for wall cooling prior to combustion. To keep the overall combustor pressure loss low the impingement pressure loss would have to be low and pressure loss from 1–2% was investigated. A high G and low pressure loss requires a low impingement X/D and 4.66 was investigated. The prediction methodology had been validated in previous publications against experimental results. Three obstacles were investigated: zig-zag rib, cylindrical pin fins and dimples in the impingement surface.

The predictions showed that the three obstacles investigated had little improvement in the surface averaged HTC compared with a smooth wall. There was a 10% benefit in HTC at low G for the cylindrical pin and zig-zag obstacles, but 10% lower HTC benefit at high G. This was because there was a considerable difference in the axial variation in the HTC. For the first 4 impingement holes in the 10 hole array the smooth was was much superior to any of the obstacle enhanced surfaces, but the obstacles increased the HTC in the downstream rows of impingement jets. The reason for this was twofold: the obstacles induced a flow maldistribution (except the dimples) so that the the smooth wall had a higher coolant mass flow for the first four

rows of holes and the obstacle walls had a higher coolant mass flow in the last four rows of holes. Also the presence of obstacles on the surface prevented the impingement action of the flow on the surface from adjacent jets, with the turbulence created at the interaction, this reduced the surface TKE and local HTC for the impingement jets with obstacles.

The dimples were predicted to make all aspects of the heat transfer worse. The surface averaged HTC was lower at all G and 26% lower at the highest G. At all axial distances the HTC was lower than for the smooth wall or any of the walls with obstacles. The reason for this was that the impingement jet aligned with the dimple resulted in deflection of the jet away from the target surface and increased the reverse flow in the gap. This reduced local TKE and HTC on the surface at all G. For the downstream holes the crssflow deflected the impingement jet to impact the target wall downstream of the dimple, so the dimple had no effect.

The CHT/CFD predictions show that for the present application of high coolant mass flux and low impingement pressure loss, with low X/D and Z/D, there is no advantage of using obstacles or dimples in the gap to enhance the target surface heat transfer. The predictions show why this occurs. Seven obstacle configurations have now been studied including previous work [15] and no significant improvement on the smooth wall impingement cooling results have been found.

ACKNOWLEDGEMENTS

Abubakar M. El-jummah wishes to acknowledge the financial support from University of Maiduguri and the Government of Nigeria for a PhD scholarship.

NOMENCLATURE

A	Impingement hole porosity = $((\pi/4)\ D^2)/X^2$
D	Impingement air hole diameter, m
D_o	Obstacle diameter, m
G	Coolant Mass flux, kg/sm^{2}bara
h	Heat transfer coefficient (HTC), W/m^{2}K
H	Obstacle height, m
k_f	Thermal conductivity of fluid, W/mK
L	Test wall metal thickness, m
n	Number of jet/effusion hole/unit surface area, m^{-2}
N	Number of upstream rows of impingement holes
Nu	Nusselt Number
ρ	Density of air, kg/m^3
ΔP	Impingement wall pressure loss, Pa
P	Coolant supply static pressure (approx. 1bar)
Pr	Prandtl number
Re	Reynolds number
t	Obstacle thickness, m
T_∞	Coolant temperature, 288K
T^*	Normalized mean temperature
T_S	Target surface metal wall temperature, K
T_w	Target wall imposed temperature (360K)
V_j	Impingement jet mean velocity, m/s
ν	Kinematic viscosity, m^2/s
W	Obstacle width, m
X	Hole to hole pitch, m
y^+	Inner variable wall normal coordinate ($\xi U\tau/\nu$)
Z	Plate to plate gap, m
ξ	Grid cell size, m
δ	Obstacle depth, m

Subscripts

avg	average
L	Local
C	cross-flow
j	Jet
W	Wall
s	Surface
∞	Coolant
f	fluid
o	Obstacle

REFERENCES

[1] Wang Z., Ireland P. T., Kohler S. T. and Chew J. W. 1998. Heat Transfer Measurements to a Gas Turbine Cooling Passage With Inclined Ribs. *Trans. ASME J. Turbomachinery,* 120**,** 63 - 69.

[2] Reiss F., Wiers S-H., Orth U., Aschenbruck E., Lauer M. and El Masalme J. 2014. Combustion System Development and Testing for MAN's New Industrial Gas Turbines MGT 6100 and MGT 6200. *Proc. ASME Turbo Expo,* ASME Paper GT2014-25907**,** 1 - 9.

[3] Abdul Husain R. A. A. and Andrews G. E. 1991. Enhanced Full Coverage Impingement Heat Transfer With Obstacle in the Gap. *Proc. ASME Int. Gas Turbine & Aeroengine Congress & Eposition,* 91-GT-346**,** 1 - 12.

[4] Shizuya M. and Kawaike K. 1987. Experimental Investigation of Blade Internal Cooling Methods Using Ribs and Fins. *Proc. GTSJ Int. Gas Turbine Congress,* IGTC-65**,** 159 - 166.

[5] Xie Y., Li P., Lan J. and Zhang D. 2013. Flow and Heat Transfer Characteristics of Single Jet Impinging on Dimpled Surface *Trans. ASME J. Heat Transfer,* 135**,** 1 - 15.

[6] Azad G. S., Huang Y. and Han J. C. 2000. Impingement Heat Transfer on Dimpled Surfaces Using a Transient Liquid Crystal Technique. *AIAA J. Thermophysics and Heat Transfer,* 14 (2)**,** 186 -193.

[7] Kanokjaruvijit K. and Martinez-Botas R. F. 2003. Jet Impingement onto a Dimpled Surface With Different Cross-Flow Schemes. *Proc. GTSJ Int. Gas Turbine Congress,* IGTC TS-074**,** 1 - 8.

[8] Kanokjaruvijit K. and Martinez-Botas R. F. 2005. Heat Transfer and Pressure Investigation of Dimple Impingement. *Proc. ASME Turbo Expo,* ASME Paper GT2005-68823**,** 1 - 12.

[9] Kanokjaruvijit K. and Martinez-Botas R. F. 2005. Parametric Effects on Heat Transfer of Impingement on Dimpled Surface. *Trans. ASME J. Turbomachinery,* 127**,** 287 - 296.

[10] Kanokjaruvijit K. and Martinez-Botas R. F. 2005. Jet Impingement on a Dimpled Surface With Different Cross-Flow Schemes. *Elsevier Int. J. Heat and Mass Transfer,* 48**,** 161 - 170.

[11] Ireland P. T., Neely A. J., Gillespie D. R. H. and Robertson A. J. 1999. Turbulent Heat Transfer Measurements using Liquid Crystals. *Elsevier. Int. J. Heat and Fluid Flow,* 20**,** 355 - 367.

[12] Azad G. M. S., Huang Y. and Han J. 2002. Jet Impingement Heat Transfer on Pinned Surfaces Using a Transient Liquid Crystal Technique. *Int. J. Rotating Machinery,* 8 (3)**,** 161 - 173.

[13] Feng X., Tian S., Bai J., Zhang H., Wang K. and Wang H. 2014. Numerical Investigation of an Integrated Impingement and Pin_Fin Cooling Configuration in a Wedge Duct. *Proc. ASME Turbo Expo,* ASME Paper GT2014-26185**,** 1 - 10.

[14] Sparrow E. M., Ramsey J. W. and Altemani C. A. C. 1980. Experiments on In-line Pin-Fin Arrays and Performance Comparisons With Staggered Arrays. *Trans. ASME J. Heat Transfer,* 102**,** 44 - 50.

[15] El-jummah A. M., Andrews G. E. and Staggs J. E. J. 2018. Enhancement of Impingement Heat Transfer with the Cross-flow Normal to Ribs and Pins between each Row of Holes. *Proc. ASME Turbo Expo: Turbomachinery Technical Conference and Exposition,* ASME Paper GT2018-76969**,** 1-12.

[16] El-jummah A. M., Oluwole F. A., Andrews G. E. and Staggs J. E. J. 2017. Numerical Predictions of Enhanced Impingement Jet Cooling with Ribs and Pin Fin in Co-flow and Cross-flow Configurations. *Arid Zone Journal of Engineering, Technology and Environment (AZOJETE),* Vol. 13 (1)**,** 149 - 162.

[17] El-jummah A. M., Andrews G. E. and Staggs J. E. J. 2016. Impingement Jet Cooling with Ribs and Pin Fin Obstacles in Co-flow Configurations: Conjugate Heat Transfer Computational Fluid Dynamic Predictions. *Proc. ASME Turbo Expo: Turbomachinery Technical Conference & Exposition,* ASME Paper GT2016-57021**,** 1-15.

[18] Andrews G. E., Abdul Husain R. A. A. and Mkpadi M. C. 2003. Enhanced Impingement Heat Transfer: Comparison of Co-Flow and Cross-flow with Rib Turbulators. *Proc. GTSJ Int. Gas Turbine Congress,* IGTC TS-075 1 - 8.

[19] Andrews G. E., Abdul Husain R. A. A. and Mkpadi M. C. 2006. Enhanced Impingement Heat Transfer: The Influence of Impingement X/D for Interrupted Rib Obstacles (Rectangular Pin Fins). *Trans. ASME J. Turbomachinery,* 128**,** 321 - 331.

[20] El-jummah A. M., Abdul Hussain R. A. A., Andrews G. E. and Staggs J. E. J. 2014. Conjugate Heat Transfer Computational Fluid Dynamic Predictions of Impingement Heat Transfer: The Influence of Hole Pitch to Diameter Ratio X/D at Constant Impingement Gap Z. *Trans. ASME J. Turbomachinery,* 136 (12)**,** 1-16.

[21] El-jummah, A. M., Abdul Hussain R. A. A., Andrews G. E. and Staggs J. E. J. 2013. Conjugate Heat Transfer CFD Predictions of the Surface Averaged Impingement Heat Transfer Coefficients for Impingement Cooling with Backside Cross-flow. *Proc. ASME IMECE Conference,* IMECE-63580**,** 1 - 14.

[22] El-jummah A. M., Abdul Hussain R. A. A., Andrews G. E. and Staggs J. E. J. 2014. Conjugate Heat Transfer CFD Predictions of Impingement Heat Transfer: Influence of the Number of Holes for a Constant Pitch to Diameter Ratio X/D. *Proc. ASME Gas Turbine Conference,* ASME Paper GT2014-25268**,** 1-14.

[23] El-jummah, A. M., Andrews, G. E. and Staggs, J. E. J. 2013. Conjugate Heat Transfer CFD Predictions of Impingement Jet Array Flat Wall Cooling Aerodynamics with Single Sided Flow Exit. *Proc. ASME Turbo Expo Conference,* ASME Paper GT2013-95343**,** 1-12.